

This is a pre print version of the following article:

Numerical study of submerged impinging jets for power electronics cooling / Sabato, Massimo; Fregni, Andrea; Stalio, Enrico; Brusiani, Federico; Tranchero, Maurizio; Baritaud, Thierry. - In: INTERNATIONAL JOURNAL OF HEAT AND MASS TRANSFER. - ISSN 0017-9310. - 141:(2019), pp. 707-718. [10.1016/j.ijheatmasstransfer.2019.06.081]

Terms of use:

The terms and conditions for the reuse of this version of the manuscript are specified in the publishing policy. For all terms of use and more information see the publisher's website.

01/01/2026 21:58

Numerical Study of Submerged Impinging Jets for Power Electronics Cooling

Massimo Sabato^a, Andrea Fregni^a, Enrico Stalio^a, Federico Brusiani^b,
Maurizio Tranchero^b, Thierry Baritaud^b

^a*Dipartimento di Ingegneria Enzo Ferrari, Università di Modena e Reggio Emilia, via
Pietro Vivarelli 10, 41125 Modena, Italy*

^b*Ferrari S.p.A., via Enzo Ferrari, 27, 41053 Maranello, Italy*

Abstract

Advancements in power electronic technologies require devices which are small, reliable and capable of handling large power levels. Despite efficiencies of electronic components are usually above 90%, wasted thermal powers can result in heat flux densities in the order of hundreds of W/cm².

To avoid degradation in performance and lifetime of these electronic devices, specific active cooling systems need to be adopted and submerged impinging jets represent one of the most promising solutions. In the present paper a numerical study of different cooling jet configurations is presented, and high-efficiency solutions are sought. The configurations investigated are obtained by varying nozzle diameter, aspect ratio, arrangement and number of jets. Simulations are performed on a simplified computational domain which involves a single rectangular chip (representing the heat source) separated from the coolant by a multi-material solid stack.

As compared to more classical solutions like pin fins, submerged impinging jets represent an efficient technique for the cooling of power electronics. Heat is exchanged at low pumping power level. Array of jets are flexible in terms of geometry and can be specifically designed to control temperatures in critical spots.

Keywords: Impinging jets, Heat transfer, Power Electronics, Nozzle

Email address: enrico.stalio@unimore.it (Enrico Stalio)

Preprint submitted to International Journal of Heat and Mass Transfer *May 3, 2019*

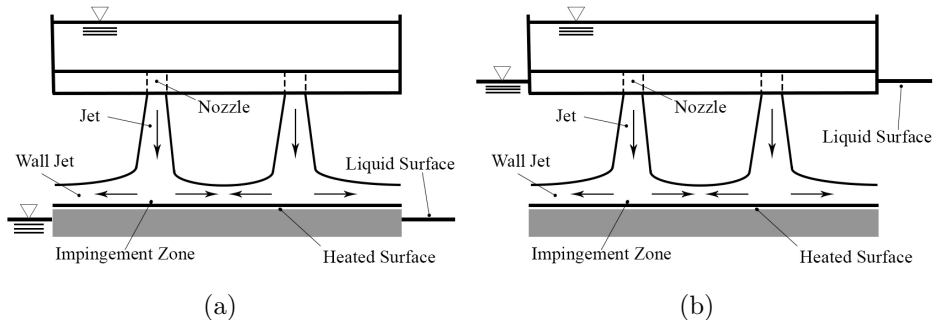


Figure 1: Impinging jets categories: (a) free-surface jet impingement, (b) submerged jet impingement [2].

1. Introduction

Heat removal techniques from power electronic devices are gaining importance in many industrial fields, including the recent applications of power electronics in hybrid and electric traction systems [1]. To tackle this technical problem, dedicated cooling systems need to be adopted and arrays of impinging jets are promising solutions because, as discussed in several papers [2, 3], they efficiently exchange large amounts of heat. On the other hand, impinging jets have been satisfactorily used from decades in several applications such as gas turbine cooling [4], glass plate tempering [5], and in deicing systems for aircrafts [6].

Generally, impinging liquid jets are divided in two categories: free-surface impinging jets (figure 1a) and submerged impinging jets (figure 1b). In the free-surface configuration liquid jets are discharged into a gaseous environment, while in the submerged configuration they are completely surrounded by the same fluid. In both cases the fluid is discharged across nozzle orifices manufactured on a plate and impinges normally on the heated surface.

Cooling performance of impinging jets strongly depends on geometrical characteristics of the nozzles such as diameter d_n , shape and aspect ratio $AR = L/d_n$ (where L is the nozzle length), as well as the number of jets and their arrangement. Diameter effect was investigated by Garimella and Naylor [7]: for a given Reynolds number and all the other parameters kept constant, turbulence intensity near the jet centreline is higher for nozzles of larger diameters. Similar results were found by Kataoka et al. [8]. Womac et al. [9] found that for a given flow rate, heat transfer improved by an increase in jet velocity (smaller diameter). Hollworth et al. [10] found that

the potential core length in turbulent jets changes with the nozzle shape. Influence of the nozzle shape was investigated also by Ronye and Dey [11]: the presence of a chamfer at the inlet leads to higher average heat transfer coefficients and lower pressure drops with respect to sharp-edge nozzles, given the same flow rate. A thorough investigation involving aspect ratio effects was carried out by Garimella and Nenaydykh [7], for $AR < 1$, heat transfer coefficient is the highest. For aspect ratios $1 \leq AR \leq 4$ the heat transfer coefficient drops sharply, but in the interval $8 \leq AR \leq 12$ it gradually increases. This behaviour can be ascribed to the flow separation and reattachment in the nozzle, and its effect on exit velocity profiles. Several researchers investigated the effect of the jet-to-target spacing H . As proposed by Churchill and Usagi [12], the heat transfer coefficient progressively grows with H/d_n and a peak is detected for $H/d_n = 5$. Gardon and Akfirat [13] report that heat transfer enhancement for increasing jet-to-target spacing is due to a turbulence increase in the mixing region. Garimella et al. [7] observed over a wide range of Reynolds numbers that for H/d_n increasing from 1 to about 4, the Nusselt number at the stagnation point remains almost constant. Analogous considerations are reported in refs. [14, 15, 16].

In the present paper, the effectiveness of impinging jet arrays for cooling electronic devices is assessed by performing a set of three-dimensional conjugated heat transfer simulations. The adopted numerical procedure is validated against experimental and numerical data reported in refs. [17] and [18]. The mesh size is determined by a grid independence procedure. Results are compared and discussed in order to obtain the best compromise in terms of cooling efficiency and pumping power required to feed the cooling system. Three nozzle diameters are considered, associated with two different aspect ratios $AR = 1$ and $AR = 0.5$, respectively. Both inline and staggered arrangements are tested and an increase in nozzles number is also taken into account. Chip heat generation rate and coolant inlet temperature are the same for all the simulated configurations. Also, each analysis is computed under the same pressure drop. This is done in view of numerical considerations and following a similar procedure as in refs. [17] and [18].

2. Computational method

Results reported in the present paper are obtained through numerical simulations performed by the open source software OpenFOAM[®]. The specific solver employed is the *chtMultiRegionSimpleFoam*, a steady-state solver

which imposes mass conservation through the SIMPLE algorithm and allows for the simulation of conjugate heat transfer cases. A second order central scheme is used for spatial discretisation of the diffusive term, while a first order upwind scheme is employed for advection.

Turbulent stresses and turbulent heat fluxes are represented by an eddy viscosity approach in a RANS context. As the Reynolds number based on the jet velocity and the jet diameter is transitional in all cases considered, a turbulence model is employed relying on the fact that in regions of low turbulence level the computed eddy viscosity is close to zero. The specific turbulence model employed in the present work is selected according to the results of a validation test performed on a single-jet configuration and reported in § 4. Comparison of the single jet results obtained using the SST $k - \omega$ and the $k - \varepsilon$ turbulence models suggests that SST $k - \omega$ model is more accurate, while the $k - \varepsilon$ model overestimates heat transfer rates in the impingement and reattachment regions. Thus, in this work turbulence is represented by the SST $k - \omega$ model.

A structured, hexahedral mesh is employed in all the simulations. To avoid the use of wall functions, meshes used are built so that the maximum distance between the centroid of the first computational cell and the wall is less than 3 wall units ($y_{w,\max}^+ < 3$), while the average distance $y_{w,\text{avg}}^+ \leq 1$ for each simulation. The size of control volumes in solid regions is larger than in the fluid region because of the smooth behaviour of temperature in solids. However the interfaces between different regions are conformal in order to avoid interpolation errors.

In this work viscous dissipation and buoyancy effects are neglected. These hypotheses are confirmed by appropriate, preliminary analyses.

3. Data reduction

The Performance Evaluation Criteria (PEC) used to assess the performances of the jet configurations are the following:

- overall heat transfer coefficient \bar{h} ;
- thermal resistance R_{th} ;
- pumping power P_p .

The overall heat transfer coefficient \bar{h} is defined as

$$\bar{h} = \frac{\dot{Q}}{A_w ([T_w] - T_{b,in})} \quad (1)$$

where \dot{Q} is the heat transferred from the chip to the coolant in the time unit, A_w is the surface extension of the solid-liquid interface, $[T_w]$ is the average temperature of this interface, and $T_{b,in}$ is the bulk temperature of the coolant at the inlet. In addition, distributions of local heat transfer coefficient

$$h = \frac{\dot{Q}}{A_w (T_w - T_{b,in})} \quad (2)$$

are computed on the impingement plates in order to provide maps of heat transfer rates. Maps are presented by normalising the local heat transfer coefficient for easier comparison

$$h^* = \frac{h - h_{\min}}{h_{\max} - h_{\min}} \quad (3)$$

In equation (3) h_{\max} and h_{\min} represent the maximum and minimum values of h among all the configurations studied.

The overall thermal resistance R_{th} between chip and coolant is defined using the temperature difference between the maximum chip temperature T_{\max} and the coolant inlet bulk temperature, as in ref. [19]

$$R_{th} = \frac{T_{\max} - T_{b,in}}{\dot{Q}} \quad (4)$$

The mechanical energy per time unit required for maintaining the flow of the coolant is calculated as

$$P_p = \dot{V} \Delta p \quad (5)$$

where \dot{V} is the volumetric flow rate and Δp is the pressure drop between the inlet and the outlet sections, $\Delta p = p_{in} - p_{out}$.

To preserve confidentiality of configurations and conditions, data are presented in a normalised form (indicated by *) using reference quantities defined as follows. The reference length is

$$l_{\text{ref}} = \sqrt{l_1 l_2} \quad (6)$$

where $l_1 l_2 = A$ is the chip plan area. The reference velocity definition is based upon the imposed pressure drop Δp and the fluid density $\rho = \rho_{\text{ref}} = 978 \text{ kg/m}^3$

$$u_{\text{ref}} = \sqrt{2 \Delta p / \rho} \quad (7)$$

while the reference temperature is

$$T_{\text{ref}} = \frac{P_0}{\rho u_{\text{ref}} l_{\text{ref}}^2 c} \quad (8)$$

In this equation P_0 is the heat generation rate of the chip and $c = c_{\text{ref}} = 4187 \text{ J/(kg K)}$ is the specific heat. Both P_0 and c are kept constant in this study.

Configurations are compared using the normalised form of thermal resistance, overall heat transfer coefficient and pumping power

$$R_{th}^* = \frac{R_{th}}{R_{th,\text{ref}}} \quad \bar{h}^* = \frac{\bar{h}}{\bar{h}_{\text{ref}}} \quad P_p^* = \frac{P_p}{P_{\text{ref}}} \quad (9)$$

Reference quantities in equation (9) are defined from those in equations (6), (7) and (8)

$$R_{th,\text{ref}} = \frac{T_{\text{ref}}}{P_{\text{ref}}} \quad \bar{h}_{\text{ref}} = \frac{P_{\text{ref}}}{T_{\text{ref}} l_{\text{ref}}^2} \quad P_{\text{ref}} = \rho l_{\text{ref}}^2 u_{\text{ref}}^3 \quad (10)$$

4. Test case validation

Prior to the study of jet arrays, the numerical procedure has been assessed and tuned. Validation is performed by comparing results on a single axisymmetric jet case against experimental and numerical results reported in refs. [17] and [18]. The validation case involves a jet of diameter $d_n = 3.18 \text{ mm}$ impinging on a flat plate heated uniformly by a constant heat flux equal to $\dot{q} = 25 \text{ W/cm}^2$. Simulations are conducted resorting to an axisymmetric model. Details on domain dimensions and boundary conditions can be found in ref. [18].

Two turbulence models are compared, the $k - \varepsilon$ and the SST $k - \omega$, in both cases no specific wall treatment is included. The average and maximum distance of the first computational point from the wall are respectively $y_{w,\text{avg}}^+ = 0.9$ and $y_{w,\text{max}}^+ = 2.9$. The radial profiles of the local heat transfer coefficient on the impingement plate are reported in figure 2, where they are compared with experimental results in ref. [17]. It appears that the SST

Table 1: Comparison between results obtained with $k - \varepsilon$ and SST $k - \omega$ turbulence models. Reference experimental and numerical data are taken from paper [18].

	$k - \varepsilon$	SST $k - \omega$	Experiment [18]	Simulation [18]
Pressure drop (Pa)	7116	7116	7116	7500
Mass flow rate (kg/s)	0.0288	0.0310	0.0326	0.0326
Discharge coefficient	0.713	0.768	0.806	-
Reattachment length	-	0.92 d_n	-	0.80 d_n

$k - \omega$ model reproduces experimental data more accurately than the $k - \varepsilon$ model. The comparison between present results and data from ref. [18] is summarised in table 1. Mass flow rate, reattachment point position and discharge coefficient are predicted by the SST $k - \omega$ model more accurately than by the $k - \varepsilon$ model. The discharge coefficient is calculated by

$$C_d = \frac{\dot{m}_r}{\dot{m}_{id}} = \frac{\dot{m}_r}{N\pi d_n^2} \sqrt{\frac{8}{\rho \Delta p}} \quad (11)$$

where \dot{m}_r represents the computed mass flow rate and \dot{m}_{id} is the mass flow rate after Bernoulli. N and d_n are the number of jets and their diameter, Δp is the imposed pressure drop between inlet and outlet and ρ is the fluid density.

Tests are performed also to check that previous results are independent of the computational grid and for assessing the influence of a fillet at the nozzle entrance. These analyses are both carried out employing the SST $k - \omega$ turbulence model.

The grid sensitivity analysis involves three meshes of increasing mesh density: \mathcal{G}_1 , \mathcal{G}_2 (used to obtain results presented above) and \mathcal{G}_3 , which respectively include 8×10^3 , 40×10^3 and 80×10^3 control volumes. In figure 3 the profiles of heat transfer coefficient obtained with different computational grids are compared, together with experimental data from ref. [17]. The profile computed on the coarse grid \mathcal{G}_1 is closer to experimental results than \mathcal{G}_2 and \mathcal{G}_3 but it shows to be grid-dependent. Instead grids \mathcal{G}_2 and \mathcal{G}_3 provide essentially the same results, and these are deemed to be non-dependent upon the spatial discretisation. The same outcome arises from the comparison of fluid dynamic parameters reported in table 2, where the reattachment length for coarse simulation is not reported since the wall-normal derivative

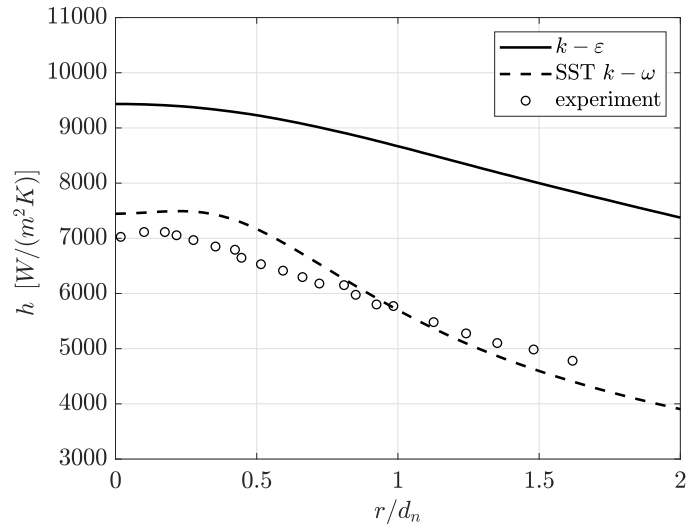


Figure 2: Radial profiles of local heat transfer coefficient on the impingement plate in the axisymmetric jet simulation: comparison between present results obtained with $k - \varepsilon$ and SST $k - \omega$ turbulence models and experimental data from ref. [17].

of the streamwise velocity component does not display a clear behaviour in the nozzle.

The influence of a fillet at the nozzle entrance is also assessed. The selected fillet radius is $R = 0.04$ mm, this value being typical for holes obtained by laser drilling. Figures 4a and 4b show the computational grids around the nozzle for the configurations with and without fillet. Results obtained in the two configurations are reported in figure 5 and table 3, where these are also compared against data reported in papers [17] and [18]. The filleted configuration provides results closer to the experiment than the sharp-edged nozzle, both in terms of heat transfer and fluid dynamic parameters. The mass flow rate increase and the different discharge coefficient are to be ascribed to the reduction in adverse pressure gradient. This effect motivates also the shorter separation length.

On the basis of the results obtained on the test case, the SST $k - \omega$ is adopted in the present study. A sharp-edged configuration is selected as results are sufficiently close to the experiments, while keeping the geometry more general.

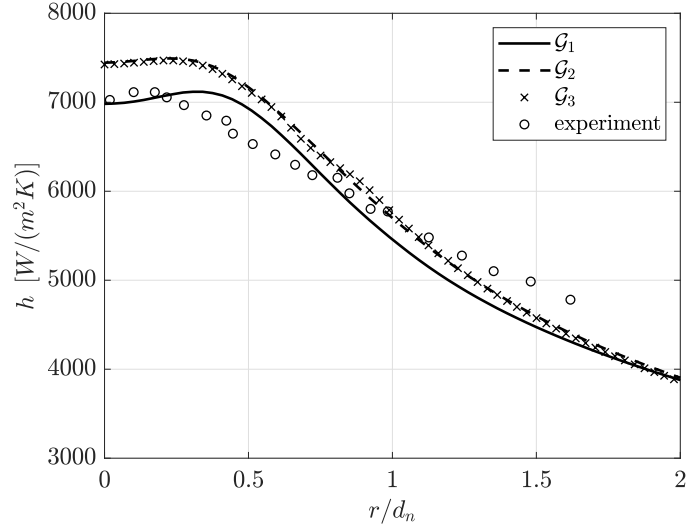
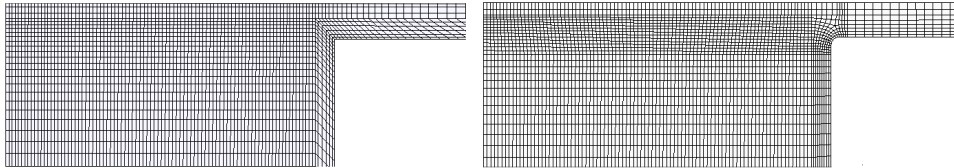


Figure 3: Radial profiles of local heat transfer coefficient on the impingement plate in the axisymmetric jet simulation: comparison between results obtained with different computational grids and experimental data from ref. [17].

Table 2: Comparison between fluid dynamic parameters obtained with different computational grids.

	\mathcal{G}_1	\mathcal{G}_2	\mathcal{G}_3
Pressure drop (Pa)	7116	7116	7116
Mass flow rate (kg/s)	0.0318	0.0310	0.0311
Discharge coefficient	0.787	0.768	0.770
Reattachment length	-	$0.92 d_n$	$0.91 d_n$



(a)

(b)

Figure 4: Computational grids in the nozzle region of the axisymmetric jet simulation: (a) sharp-edge nozzle, (b) filleted nozzle.

Table 3: Comparison between results on the sharp-edge and filleted nozzle configurations, with reference data from paper [18].

	Sharp-edge	Filleted	Experiment [18]	Simulation [18]
Pressure drop (Pa)	7116	7116	7116	7500
Mass flow rate (kg/s)	0.0310	0.0323	0.0326	0.0326
Discharge coefficient	0.768	0.800	0.806	-
Reattachment length	$0.92 d_n$	$0.75 d_n$	-	$0.80 d_n$

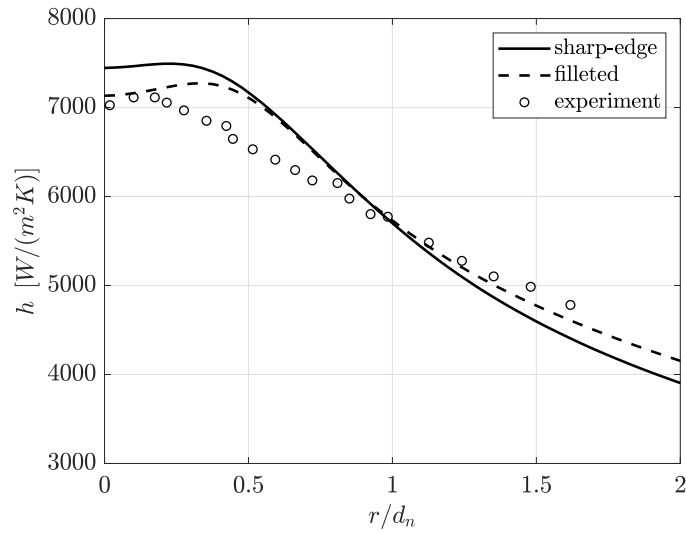


Figure 5: Radial profiles of local heat transfer coefficient on the impingement plate in the axisymmetric jet simulation: comparison between results obtained on the sharp-edge and filleted configurations and experimental data from ref. [17].

5. Description of simulated cases

The simulation campaign is conducted to investigate the behaviour of cooling performance and pumping power over a range of geometrical parameters. The arrangement and number of jets N , their diameter d_n^* , and the ratio between nozzle length L and diameter $AR = L/d_n$ are assigned as shown in table 4, which summarises all configurations investigated. Suggestions on promising configurations are taken from refs. [7, 11, 20, 14, 15, 16]. The configuration name, in the first column of table 4, is descriptive of the main geometric features. The capital letter indicates the nozzle diameter, L stands for “large” diameter, A for “average” and S for “small”, while the number corresponds to the total number of jets. When present, “s” indicates that jets are staggered and “b” marks the $AR = 0.5$ geometries. The inline and staggered configurations are indicated by $N \times N$ and $N \times N - M \times M$ respectively, where $M = N - 1$ because each staggered configuration is obtained by addition of a $M \times M$ array to the initial, coarser $N \times N$ array. Notice that the nozzle-to-target distance H is set to 3 times the nozzle diameter in all cases. This is done in order to reduce the degrees of freedom of impinging-jet configurations and because the ratio $H/d_n = 3$ is deemed near optimal, as reported in refs. [7], [2] and [20].

The computational domain is depicted in figure 6a is composed by a stack of different solid and fluid regions: a chip (which is the volumetric heat source), two layers of copper and ceramic, an aluminium plate and the coolant region, which includes an inlet plenum, the nozzles and a discharge zone. The copper, ceramic, and aluminium layers oppose a conductive thermal resistance to the heat flux per unit area of $R'_{co} = 8.44 \times 10^{-4} R'_{ref}$, $R'_{ce} = 3.66 \times 10^{-3} R'_{ref}$ and $R'_{al} = 1.55 \times 10^{-2} R'_{ref}$ respectively, where R'_{ref} is the reference thermal resistance for the heat flux per unit area, $R'_{ref} = (T_{ref} l_{ref}^2)/P_{ref}$. Geometrical and thermal properties of solid regions are held constant among all the configurations studied for keeping the same thermal conditions at the solid-liquid interface, see ref. [21] about this topic.

As shown in figure 6a, the configuration is symmetric about two planes, and only one quarter of the geometry considered is actually simulated. A (x, y) section of the nozzle plate is displayed in figure 6b.

The coolant enters the domain by the lateral boundaries of the inlet plenum at the fixed temperature $T_{in}^* = 857$, passes through the nozzles, exchanges heat from the aluminium plate and exits through the lateral boundaries of the discharge zone. The mechanical energy per unit time for main-

Table 4: Summary of configurations investigated. The nozzle diameter d_n is made non-dimensional using the reference length l_{ref} , defined in equation (6).

Test	d_n^*	disposition	N	arrangement	AR	H/d_n
L9	0.100	3×3	9	inline	1	3
L9b	0.100	3×3	9	inline	0.5	3
L13s	0.100	$3 \times 3_{-2} \times 2$	13	staggered	1	3
L13sb	0.100	$3 \times 3_{-2} \times 2$	13	staggered	0.5	3
A16	0.050	4×4	16	inline	1	3
A25s	0.050	$4 \times 4_{-3} \times 3$	25	staggered	1	3
A36	0.050	6×6	36	inline	1	3
A49	0.050	7×7	49	inline	1	3
A61s	0.050	$6 \times 6_{-5} \times 5$	61	staggered	1	3
A85s	0.050	$7 \times 7_{-6} \times 6$	85	staggered	1	3
S64	0.030	8×8	64	inline	1	3
S81	0.030	9×9	81	inline	1	3
S100	0.030	10×10	100	inline	1	3

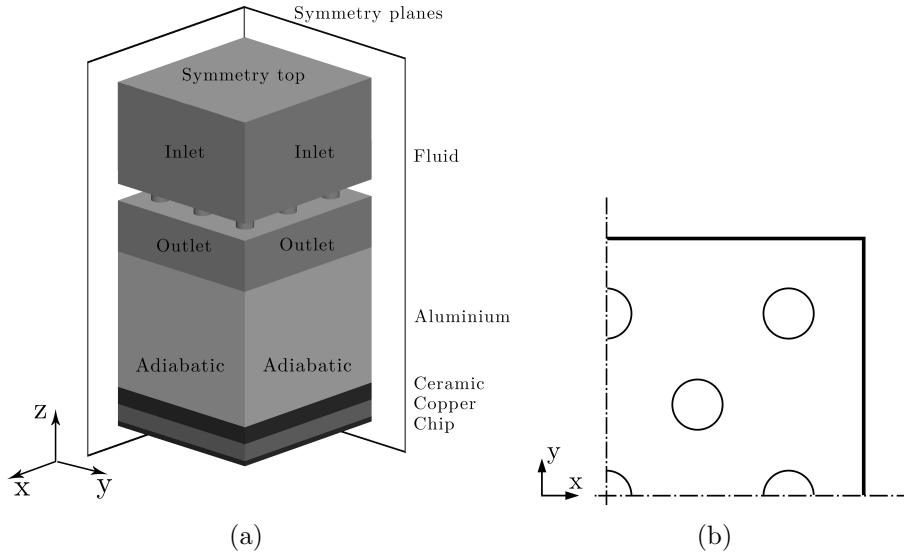


Figure 6: (a) Computational domain and boundary conditions employed in simulations, (b) (x, y) section of the nozzle plate for configurations L13s and L13sb.

taining the flow is provided by imposing a relative pressure Δp at the inlet and ambient pressure at the outlet. At the top of the inlet plenum as well as at the symmetry planes, symmetric boundary conditions are applied, while no-slip conditions are imposed at the other boundaries of the fluid region. Figure 6a shows boundary conditions on a sketch of the computational domain. The thermal input relative to the entire chip is $P_0^* = 0.025$ and is provided by setting a volumetric heat source in the chip. Heat transfer occurs exclusively in the z direction through the solid regions, and finally to the coolant; no heat is transferred through the x - or y -normal boundaries of the solid regions because these are set to adiabatic or symmetric, which at second order accuracy corresponds to the adiabatic condition.

Computational domains of the different simulations are discretised with topologically structured grids and involve from 2 to 4 million hexahedral cells. At the solid-liquid interface the mesh is conformal and a Low-Reynolds approach is adopted and checked *a posteriori*. Simulations are considered converged when the mass-flow rate and the outlet bulk temperature display a flat behaviour and residuals are below the threshold $\mathcal{R}_t = 10^{-4}$.

Heat transfer characteristics of configurations tested are analysed in section 6. Results are grouped in paragraphs by fixing the jet diameter and for variable jet configurations. An overview of heat transfer performance is provided in section 6.6, where two summarising figures are also displayed.

6. Results

6.1. Grid sensitivity analysis

In order to check that results are not grid-dependent, a grid sensitivity analysis is performed on configuration L9b using three meshes of increasing mesh density. The coarse mesh is composed by ~ 0.4 millions cells overall and each jet is discretised using 27, 28 and 50 control volumes respectively along the axial, radial and circumferential directions. The intermediate mesh is obtained by doubling the number of cells in each direction thus counting ~ 3.2 millions cells, while the fine grid is obtained by a further refinement by a factor 1.5 along the impingement direction.

Table 5 compares the PEC computed with different meshes. While on the intermediate and fine meshes almost the same results are obtained, PEC computed on the coarse mesh are somewhat different. As a consequence, configurations presented hereafter are tested using computational grids comparable with intermediate mesh.

Table 5: Comparison between results obtain with different computational grids on configuration L9b. PEC reported are defined in equations (9) and (11).

PEC	coarse	intermediate	fine
R_{th}^*	0.060	0.058	0.058
\bar{h}^*	25.42	25.25	25.21
P_p^*	0.0236	0.0250	0.0248
C_d	0.66	0.71	0.70

6.2. Aspect ratio effect

Simulations L13s and L13sb share the same configuration but have different aspect ratio: $AR = 1$ and $AR = 0.5$ respectively. These are compared in order to assess the effect of the aspect ratio. The nozzle arrangement is displayed in figure 6, where only the simulated quarter of geometry is depicted. Figures 7a and 7b display the distributions of the local heat transfer coefficient on the impingement plate of the two cases considered, where qualitatively no substantial differences can be observed. Note that these pictures display the non-dimensional heat transfer coefficient h^* only in the simulated portion of the impingement plate. Due to impingement, h^* reaches a local maximum under each jet and these regions share almost the same shape in the two cases considered. In addition, from the skewed regions of high h^* in figures 7a and 7b, it can be observed that the flow toward the lateral outlet boundaries imposes a larger deviation to the peripheral jets with respect to the central ones, as also observed in paper [22]. More local heat transfer coefficient maxima are observed in the regions where the boundary layers on the impingement plate relative to different jets interact and give place to an increase in turbulent kinetic energy, see also ref. [23]. Table 6 compares the PEC and shows that the $AR = 1$ configuration achieves a slightly higher overall heat transfer coefficient. Also the cost in terms of pumping power is about 2% higher, which indicates that the $AR = 1$ case is characterised by a slightly higher mass flow rate. Moreover, the higher discharge coefficient in the $AR = 1$ configuration denotes a better fluid dynamic efficiency.

Results presented are in agreement with refs. [11] and [20] which report of smaller pressure drops for higher aspect-ratio nozzles, which in turn lead to higher mass flow rates and higher global heat transfer coefficients when pressure is fixed at the inlet and outlet boundaries, as in present simulations.

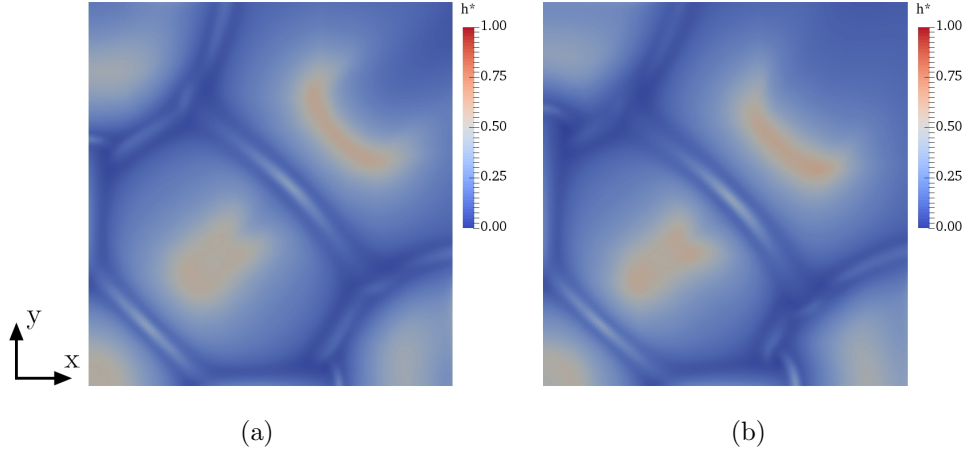


Figure 7: Normalised heat transfer coefficient on the impingement plate: (a) case L13s ($AR = 1$), (b) case L13sb ($AR = 0.5$).

Table 6: Comparison between performances of configurations L13s ($AR = 1$) and L13sb ($AR = 0.5$). PEC reported are defined in equations (9) and (11).

PEC	$AR = 0.5$	$AR = 1$
R_{th}^*	0.056	0.055
\bar{h}^*	28.37	29.23
P_p^*	0.0369	0.0377
C_d	0.72	0.74

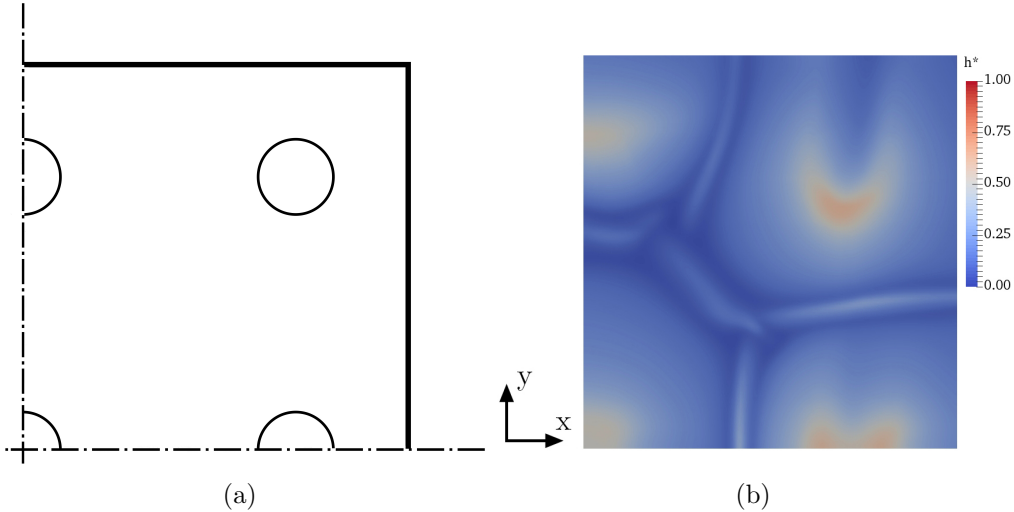


Figure 8: Configuration L9: (a) nozzle arrangement, (b) local heat transfer coefficient on the impingement plate.

On the other hand, Garimella and Nenaydykh [7] found lower heat transfer coefficients for $AR > 1$. This is only apparently in contrast with present results because in paper [7] experiments are performed with a fixed mass flow rate and the higher \bar{h}^* of the present $AR = 1$ configuration can be ascribed to a mass flow rate increase. These results together with data reported in papers [11], [20] and [7] suggest that configurations with $AR = 1$ allows to achieve better thermal performances with respect to $AR = 0.5$. Then in the following only unitary aspect ratios will be considered.

6.3. Large diameter

In this section results of configuration L9 (figure 8a) and the corresponding staggered configuration L13s (figure 6b) are compared. Figure 8b displays the distribution of local heat transfer coefficient for the L9 configuration. It can be observed that the impingement regions of the corner jets are mainly deviated along y , while in the L13s configuration deviation is almost diagonal, see figure 7a. This behaviour can be ascribed to a different interaction of the jets and a predominant direction of the flow close to the outlet sections. As reported in table 7 the overall heat transfer coefficient of the L13s configuration is around 10% higher than L9. Accordingly, lower chip temperature and lower thermal resistance are achieved by the staggered configuration, but

Table 7: Comparison between performances of configurations L9 and L13s. PEC reported are defined in equations (9) and (11).

PEC	L9	L13s
R_{th}^*	0.059	0.055
\bar{h}^*	26.41	29.23
P_p^*	0.0250	0.0377
C_d	0.71	0.74

a 34% larger pumping power is required. Performances of L13s configuration are associated with its higher mass flow rate.

6.4. Average diameter

All the configurations whose code starts with A have been designed considering the work by Womac *et al.* [9], where it is argued that a reduction in nozzles diameter improves the thermal performances of impinging jets.

The A16 configuration and the corresponding staggered one (A25s) are depicted in figures 9a and 9b, while the respective fields of local heat transfer coefficient on the impingement plates are reported in figures 10a and 10b. Since in these cases the diameter is smaller than the previous configurations, the regions of high h^* due to impingement are narrower. Moreover, the increased number of jets leads to a more intense interaction among them, particularly in the A25s case, as shown by the skewed shapes of the impingement regions.

Configurations A16 and A25s are compared to case L13s in table 8. The staggered architectures (A25s and L13s) provide comparable values of R_{th}^* and \bar{h}^* , which denote better thermal performances than configuration A16. Surprisingly this result is achieved by configuration A25s requiring less than half the pumping power required by L13s, which at given pressure drop and constant density corresponds to less than half mass flow rate. Hence case A25s is almost two times more efficient than L13s.

As apparently remarkable thermal performances can be achieved at a low cost in terms of pumping power by an increased number of jets, architectures A36, A49 and the relative staggered ones, A61s and A85s, are considered; these are sketched in figures 11a, 11b, 11c, and 11d.

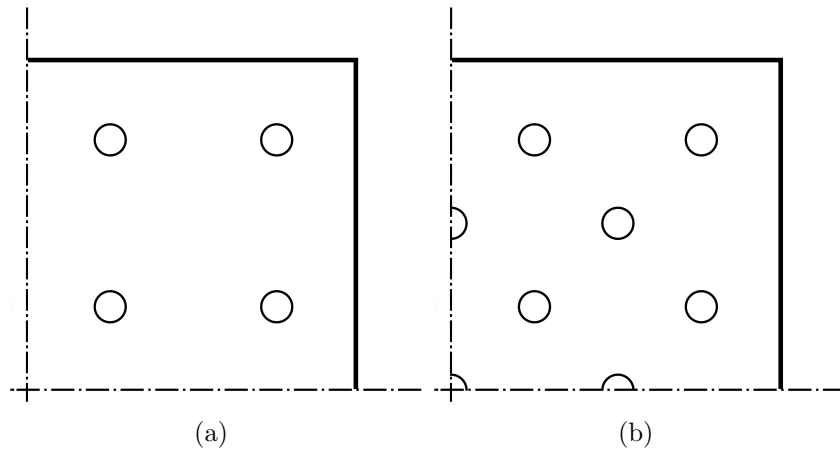


Figure 9: Nozzle plate configurations: (a) A16, (b) A25s.

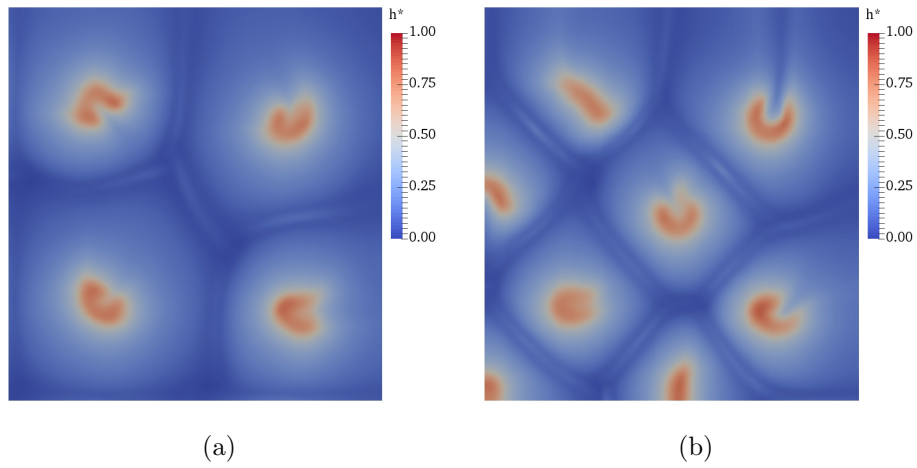


Figure 10: Normalised heat transfer coefficient on the impingement plate: (a) configuration A16, (b) configuration A25s.

Table 8: Comparison between performances of configurations A16, A25s and L13s. PEC reported are defined in equations (9) and (11).

PEC	A16	A25s	L13s
R_{th}^*	0.062	0.056	0.055
\bar{h}^*	24.56	28.66	29.23
P_p^*	0.0108	0.0168	0.0377
C_d	0.69	0.68	0.74

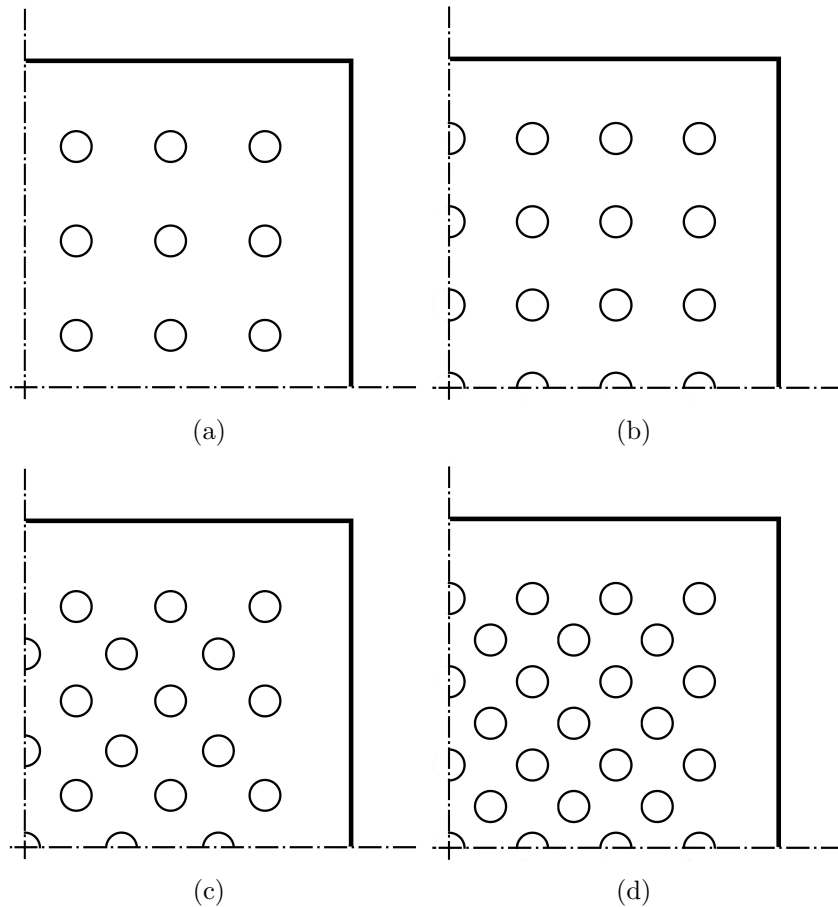


Figure 11: Nozzle plate configurations: (a) A36, (b) A49, (c) A61s, (d) A81s.

Table 9: Comparison between performances of configurations A36, A49, A61s, and A85s. PEC reported are defined in equations (9) and (11).

PEC	A36	A49	A61s	A85s
R_{th}^*	0.052	0.051	0.050	0.049
\bar{h}^*	32.13	33.60	34.43	35.12
P_p^*	0.0223	0.0275	0.0355	0.0612
C_d	0.63	0.57	0.59	0.73

Overall results are presented in table 9. The increased number of jets leads to improved thermal performances but higher pumping power requirements. In particular, configuration A85s provides a thermal resistance 14% lower than case A25s, but require a pumping power which is more than 3.5 times higher. From these results it appears that further increases in N would lead to slightly higher thermal performances but much larger requests of mechanical power. This asymptotic trend is emphasised in §6.6.

Contours of local heat transfer coefficients are presented in figures 12a, 12b, 12c and 12d, where peaks of heat transfer rate corresponding to jets close to the outlet boundaries are markedly weaker than in the central region. As already commented, this is due to the higher mass flow rate in configurations with larger N . Indeed the (x, z) and (y, z) plenum cross-sections of configurations A36, A49, A61s and A85s are the same: l_1 and l_2 are given and $H = 3d_n$ is constant when d_n is fixed, *e.g.* in “A” configurations. Therefore higher mass flow rates lead to higher velocities in the (x, y) plane, which deviate the peripheral jets from the ideal, orthogonal impingement. This phenomenon is deemed to motivate the marginal heat transfer enhancement observed in configurations A36, A49, A61s and A85s.

6.5. Small diameter

The results in the previous sections suggest that nozzles with smaller diameter provide better thermal performances, thus a further reduction of d_n might be beneficial and simulations whose code starts with S have been designed for this reason. As for large nozzle numbers the strong flow fields in the discharge plenum prevent the effective impingement of jets, a limit is sought for the total area of nozzles:

$$A_n = (N\pi d_n^2)/4 \quad (12)$$

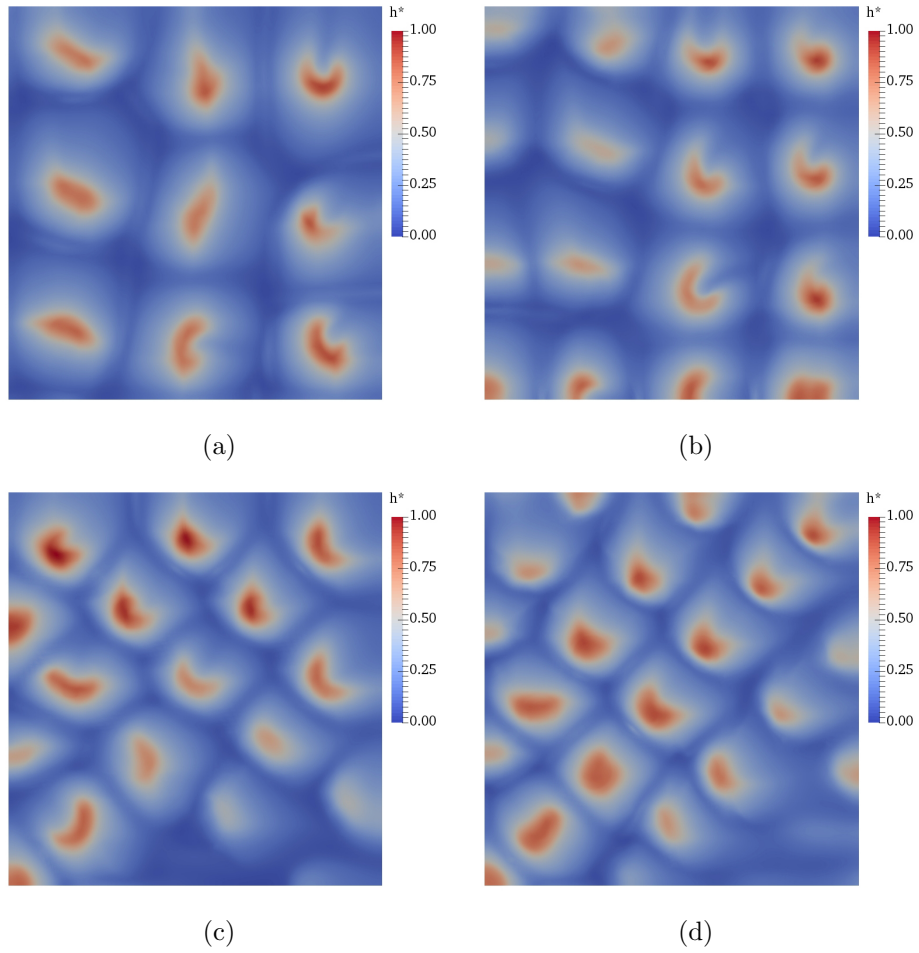


Figure 12: Normalised heat transfer coefficient on the impingement plate in configurations: (a) A36, (b) A49, (c) A61s and (d) A85s.

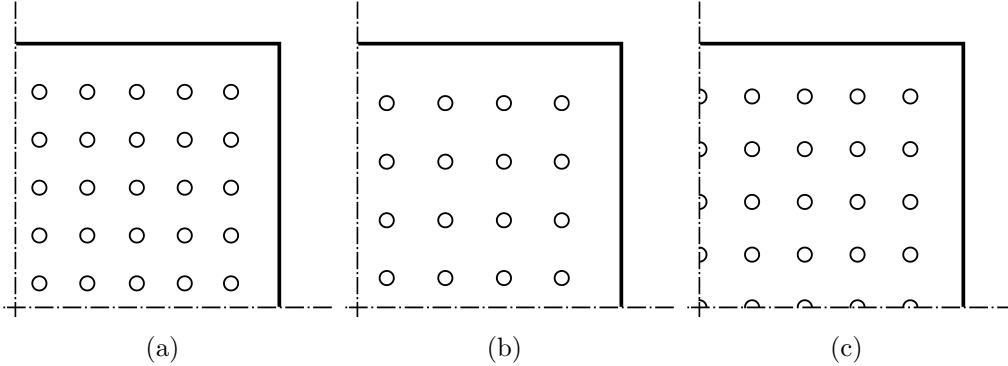


Figure 13: Nozzle plate configurations: (a) S100, (b) S64, (c) S81.

The comparison of heat transfer coefficient distributions reported in figure 12 shows qualitatively that configuration A36 allows for an almost undisturbed jet impingement. Thus its total area of nozzles, $A_n^{(A36)} = 0.09 (\pi/4) l_{\text{ref}}^2$, has been designated as the reference maximum total nozzle area allowing for an effective impingement of all jets. In order to match area $A_n^{(A36)}$ by an array of jets of diameter $d_n = 0.03 l_{\text{ref}}$ (*i.e.* the nozzles diameter in “S” configurations), one hundred jets must be employed

$$0.03^2 N (\pi/4) l_{\text{ref}}^2 = A_n^{(A36)} \Rightarrow N = 100 \quad (13)$$

Figure 13a shows configuration S100, which involves 100 nozzles arranged in a 10×10 inline array. As according to equation (13) configuration S100 is at the upper A_n limit, also configurations S64 and S81 are considered, respectively with $N=64$ and $N=81$ both arranged inline. These are displayed in figures 13b and 13c.

Distributions of h^* on the impingement plate of configurations S64, S81 and S100 are reported in figures 14a, 14b and 14c. As expected peaks related to impingement are not skewed and indicate that jets do not undergo a substantial deflection. The total nozzle area limit, set tentatively to $A_n^{(A36)}$, can then be considered as a practical indication for an effective impingement of all jets in present conditions.

The PEC of configurations with small diameter are reported in table 10, where a consistent reduction of pumping power and better thermal performances are achieved with respect to average diameter configurations. For example, the thermal resistance of configuration S100 is comparable to case A85s, but the overall heat transfer coefficient \bar{h}^* is 11% higher. Moreover, a

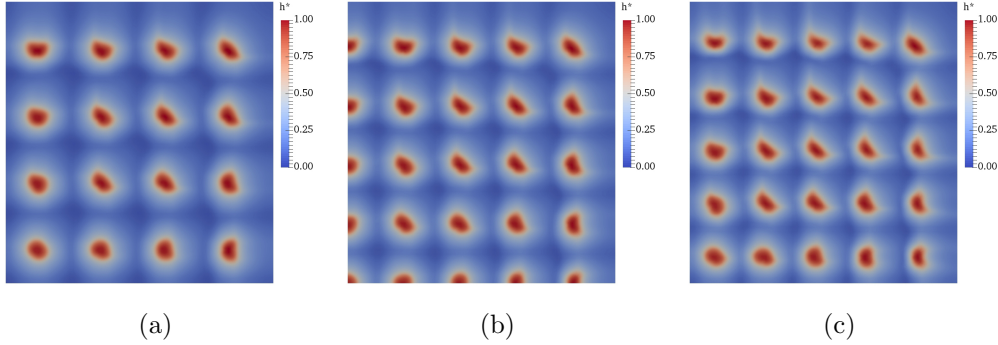


Figure 14: Normalised heat transfer coefficient on the impingement plate in configurations: (a) S64, (b) S81 and (c) S100.

Table 10: Comparison between performances of configurations S64, S81 and S100. PEC reported are defined in equations (9) and (11).

PEC	S64	S81	S100
R_{th}^*	0.051	0.049	0.047
\bar{h}^*	33.59	36.30	39.01
P_p^*	0.0147	0.0186	0.0230
C_d	0.65	0.65	0.65

2.5 times reduction in pumping power is obtained. It is clear that both pumping power and thermal performance are strongly affected by the diameter of nozzles. Comparing the S architectures it can be noticed that increasing the number of jets the thermal resistance decreases while the pumping power increases.

6.6. Discussion

Figures 15a and 15b summarise the performances of configurations investigated on charts which report R_{th}^* and \bar{h}^* as a function of P_p^* . Promising configurations are characterised by low pumping power, low thermal resistance and high overall heat transfer coefficient, therefore their operating point is placed close to the origin in chart $R_{th}^*(P_p^*)$ and in the upper-left part of chart $\bar{h}^*(P_p^*)$. It is clear that a reduction in nozzle diameters allows for lower thermal resistances (and higher overall heat transfer coefficient) and lower

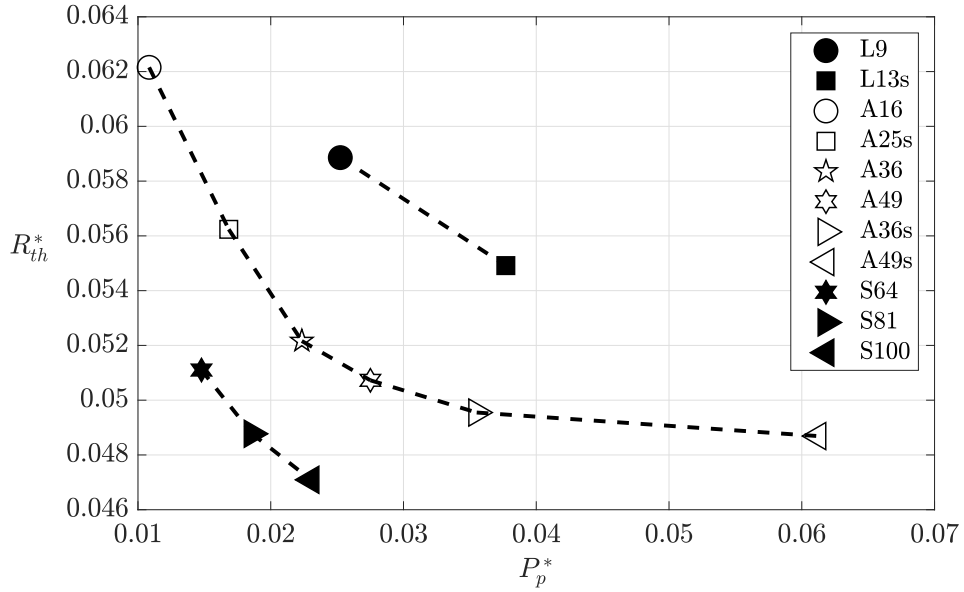
pumping powers. Since the pressure drop is the same for every configuration, a lower pumping power indicates lower mass flow rate, thus in general architectures with smaller d_n^* exchange more heat with less mass flow rate. No further reduction in nozzle diameter is considered because already the minimum d_n considered here (in the order of 0.1 mm) might cause obstructions and fouling. In addition very small diameters make heat exchangers very sensible to construction tolerances. Data pertaining to configurations with average diameter show an asymptotic behaviour: increasing the number of jets beyond a certain number leads to a pumping power increase much larger than the thermal performance enhancement, see figure 15a and 15b.

7. Conclusions

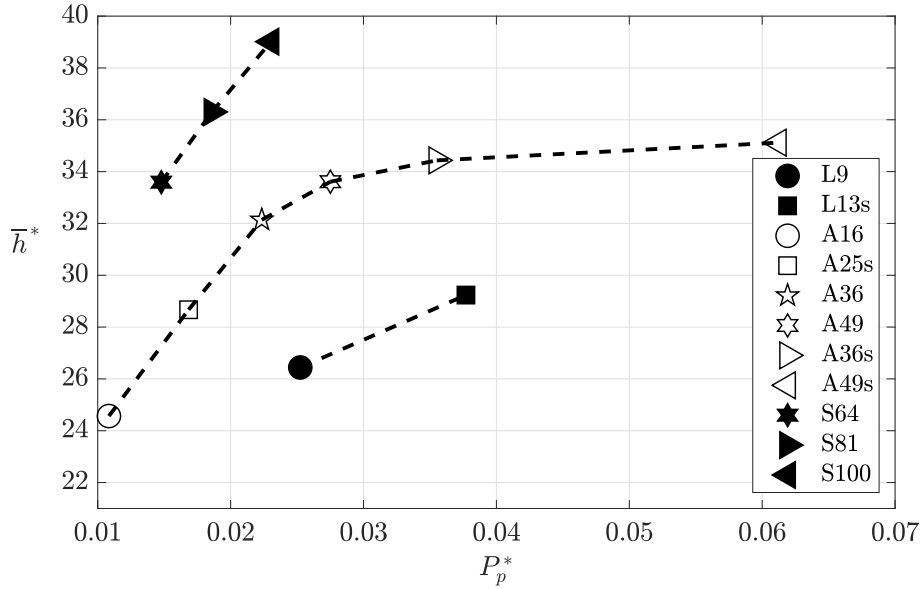
The problem of cooling power electronic components is often solved by using cooling fins [24] or heat transfer enhanced surfaces [25]. The use of impinging jets is currently recognised as a viable alternative [2, 3]. A numerical study is presented aiming at the discussion of the main parameters affecting pumping power and heat transfer effectiveness of heat sinks using arrays of impinging jets.

The numerical procedure is developed in the frame of the open-source software OpenFOAM[®], and is validated by comparing results of a single, axisymmetric jet simulation against experimental and numerical results. As a consequence of the validation procedure, the SST $k - \omega$ turbulence model is adopted. Besides validation, also a grid independence study is carried out to identify the most appropriate mesh for simulations.

Several configurations in terms of diameter, number and arrangement of nozzles are investigated, following suggestions in refs. [7, 11, 20, 14, 15, 16]. Performances of the configurations studied are summarised in figures 15a and 15b. Results show that a reduction in nozzle diameter leads to an overall heat transfer enhancement, as well as reduced pumping power requirements. However, the nozzle diameter cannot be too small, because of manufacturing tolerances and to avoid fouling and obstructions. In addition it is observed that in configurations with average nozzles diameter ($d_n = 0.050 l_{\text{ref}}$) and when the number of nozzles grows considerably, only a marginal heat transfer enhancement is achieved while the pumping power increases consistently. This is due to a mass flow rate increase which leads to higher discharge velocities directed towards the outlet boundaries, preventing the orthogonal impingement of jets. Accordingly, an asymptotic behaviour in $R_{th}^* (P_p^*)$ and



(a)



(b)

Figure 15: Summary of the investigated configurations: (a) Thermal resistance as a function of the pumping power $R_{th}^*(P_p^*)$ and (b) Heat transfer coefficient as a function of the pumping power $\bar{h}^*(P_p^*)$.

$\bar{h}^*(P_p^*)$ planes is observed. In order to limit deviating velocities in the discharge plenum, the mass flow rate across the nozzles needs to be restricted, and this can be done considering an upper limit of the total nozzle area A_n . In the present study $A_n^{(A36)}$, the total nozzle area in configuration A36, is considered as the maximum value of A_n which limits jets deviation. Results obtained in small diameter configurations, which are designed following this constraint, appear to substantiate this limit.

In summary, submerged impinging jets can exchange heat at low costs in terms of mechanical pumping power and are very flexible in terms of geometry allowing for the design heat exchangers specifically tailored to cool specific hot spots.

References

- [1] A. Carriero, M. Locatelli, K. Ramakrishnan, G. Mastinu, M. Gobbi, A review of the state of the art of electric traction motors cooling techniques, Tech. rep., SAE Technical Paper (2018).
- [2] A. Robinson, E. Schnitzler, An experimental investigation of free and submerged miniature liquid jet array impingement heat transfer, *Experimental Thermal and Fluid Science* 32 (1) (2007) 1–13.
- [3] G. J. Michna, E. A. Browne, Y. Peles, M. K. Jensen, The effect of area ratio on microjet array heat transfer, *International Journal of Heat and Mass Transfer* 54 (9-10) (2011) 1782–1790.
- [4] S. W. Chang, K.-C. Yu, Thermal performance of radially rotating trapezoidal channel with impinging jet-row, *International Journal of Heat and Mass Transfer* 136 (2019) 246–264.
- [5] M. Akcay, Experimental investigation of the relationship between heat transfer rate and number of broken glass particles in tempering process of glass plates, *Experimental Thermal and Fluid Science* 83 (2017) 260–270.
- [6] S. Caliskan, S. Baskaya, T. Calisir, Experimental and numerical investigation of geometry effects on multiple impinging air jets, *International Journal of Heat and Mass Transfer* 75 (2014) 685–703.

- [7] S. V. Garimella, B. Nenaydykh, Nozzle-geometry effects in liquid jet impingement heat transfer, *International Journal of Heat and Mass Transfer* 39 (14) (1996) 2915–2923.
- [8] K. Kataoka, M. Suguro, H. Degawa, K. Maruo, I. Mihata, The effect of surface renewal due to largescale eddies on jet impingement heat transfer, *International Journal of Heat and Mass Transfer* 30 (3) (1987) 559–567.
- [9] D. Womac, S. Ramadhyani, F. Incropera, Correlating equations for impingement cooling of small heat sources with single circular liquid jets, *Journal of heat transfer* 115 (1) (1993) 106–115.
- [10] B. Hollworth, S. Wilson, Entrainment effects on impingement heat transfer: Part imeasurements of heated jet velocity and temperature distributions and recovery temperatures on target surface, *Journal of heat transfer* 106 (4) (1984) 797–803.
- [11] A. Royne, C. J. Dey, Effect of nozzle geometry on pressure drop and heat transfer in submerged jet arrays, *International Journal of Heat and Mass Transfer* 49 (3-4) (2006) 800–804.
- [12] S. Churchill, R. Usagi, A general expression for the correlation of rates of transfer and other phenomena, *AIChE Journal* 18 (6) (1972) 1121–1128.
- [13] R. Gardon, J. C. Akfirat, The role of turbulence in determining the heat-transfer characteristics of impinging jets, *International journal of heat and mass transfer* 8 (10) (1965) 1261–1272.
- [14] C.-Y. Li, S. V. Garimella, Prandtl-number effects and generalized correlations for confined and submerged jet impingement, *International Journal of Heat and Mass Transfer* 44 (18) (2001) 3471–3480.
- [15] S. V. Garimella, R. Rice, Confined and submerged liquid jet impingement heat transfer, *Journal of Heat Transfer* 117 (4) (1995) 871–877.
- [16] S. V. Garimella, Influence of nozzle geometry on heat transfer in submerged and confined liquid jet impingement, *Proceedings of the ASME Cooling and Thermal Design of Electronic Systems*, 1995.

- [17] G. Morris, S. Garimella, R. Amano, Prediction of jet impingement heat transfer using a hybrid wall treatment with different turbulent Prandtl number functions, *Journal of heat transfer* 118 (3) (1996) 562–569.
- [18] G. K. Morris, S. V. Garimella, Orifice and impingement flow fields in confined jet impingement, *Journal of Electronic Packaging* 120 (1) (1998) 68–72.
- [19] D. B. Tuckerman, R. F. W. Pease, High-performance heat sinking for VLSI, *IEEE Electron device letters* 2 (5) (1981) 126–129.
- [20] B. P. Whelan, A. J. Robinson, Nozzle geometry effects in liquid jet array impingement, *Applied Thermal Engineering* 29 (11-12) (2009) 2211–2221.
- [21] G. Nasif, R. Balachandar, R. Barron, Conjugate analysis of wall conduction effects on the thermal characteristics of impinging jets, *International Journal of Heat and Mass Transfer* 116 (2018) 259–272.
- [22] P. S. Penumadu, A. G. Rao, Numerical investigations of heat transfer and pressure drop characteristics in multiple jet impingement system, *Applied Thermal Engineering* 110 (2017) 1511–1524.
- [23] H. Martin, Heat and mass transfer between impinging gas jets and solid surfaces, in: *Advances in heat transfer*, Vol. 13, Elsevier, 1977, pp. 1–60.
- [24] S. Ndao, Y. Peles, M. K. Jensen, Multi-objective thermal design optimization and comparative analysis of electronics cooling technologies, *International Journal of Heat and Mass Transfer* 52 (19-20) (2009) 4317–4326.
- [25] O. Errico, E. Stalio, Direct numerical simulation of turbulent forced convection in a wavy channel at low and order one Prandtl number, *International Journal of Thermal Sciences* 86 (2014) 374–386.